Cost-Effective Scalable Synthesis of Mesoporous Germanium Particles *via* a Redox-Transmetalation Reaction for High-Performance Energy Storage Devices

Sinho Choi,[†,§] Jieun Kim,[†,§] Nam-Soon Choi,[†] Min Gyu Kim,[*,‡] and Soojin Park[*,†]

[†]Department of Energy Engineering, School of Energy and Chemical Engineering, Ulsan National Institute of Science and Technology (UNIST), Ulsan 689-798, South Korea and [‡]Beamline Research Division, Pohang Accelerator Laboratory, Pohang University of Science and Technology, Pohang 790-784, South Korea. [§]These authors contributed equally to this work.

ABSTRACT Nanostructured germanium is a promising material for high-performance energy storage devices. However, synthesizing it in a cost-effective and simple manner on a large scale remains a significant challenge. Herein, we report a redox-transmetalation reaction-based route for the large-scale synthesis of mesoporous germanium particles from germanium oxide at temperatures of 420–600 °C. We could confirm that a unique redox-transmetalation reaction occurs between Zn^0 and Ge^{4+} at approximately 420 °C using temperature-dependent *in situ* X-ray absorption fine structure analysis. This reaction has several advantages, which include (i) the successful synthesis of germanium particles at a low temperature (~450 °C), (ii) the accommodation of large volume changes, owing to the mesoporous structure of the germanium particles, and (iii) the ability to synthesize the particles in a cost-effective and scalable manner, as inexpensive metal oxides are used as the starting materials. The optimized mesoporous germanium anode exhibits a reversible capacity of ~1400 mA h g^{-1} after 300 cycles at a rate of 0.5 C (corresponding to the capacity retention of 99.5%), as well as stable cycling in a full cell containing a $LiCoO_2$ cathode with a high energy density (charge capacity = 286.62 mA h cm^{-3}).

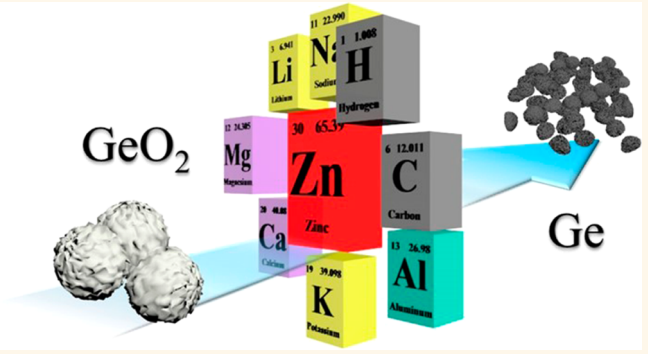

KEYWORDS: mesoporous germanium · redox-transmetalation · zincothermic reduction · germanium anode · energy storage devices

Lithium-ion batteries (LIBs), which are essential electrochemical energy storage devices, are being used to power portable electronics such as cell phones, laptops, and digital cameras, because of their advantageous properties, which include a high working voltage, high energy density, long cycling life, and the absence of the memory effect.[1−3] However, current LIBs, which consist of a graphite anode and a $LiCoO_2$ cathode, do not meet the requirements for more advanced applications such as higher energy and power densities. Thus, it is crucial to develop alternative electrode materials with higher gravimetric and volumetric capacities than those of conventional ones.[4,5] For example, in the case of a 18650 cell consisting of a graphite anode with a capacity of 372 mA h g^{-1} and a $LiCoO_2$ cathode with a capacity of ~137 mA h g^{-1}, if a graphite anode is replaced with an anode of a lithium-alloying material having a capacity greater than 1000 mA h g^{-1}, the total battery capacity would increase by more than 20%.[6,7] For this reason, Si and Ge are attracted increasing attention as promising high-capacity anode materials.

Even though Ge is more expensive than Si and thus has attracted less attention, the fact that Ge is as abundant as Si in the earth's crust suggests that Ge-based materials can be used for LIB anodes.[8] Furthermore, Ge has several advantages over Si. Although the gravimetric capacity of Ge at

* Address correspondence to spark@unist.ac.kr (S.P.), mgkim@postech.ac.kr (M.G.K.).

Received for review January 18, 2015 and accepted February 9, 2015.

Published online February 09, 2015
10.1021/acsnano.5b00389

room temperature (1384 mA h g^{-1} in the form of $Li_{15}Ge_4$) is much lower than that of Si at room temperature (3579 mA h g^{-1}), the volumetric capacity of Ge (7366 A h cm^{-3}) is second only to that of Si (8334 A h cm^{-3}).[9] In addition, Ge exhibits high electrical conductivity (10^4 times higher than that of Si), owing to its small band gap, which is 0.6 eV,[10,11] and exceptionally high lithium-ion diffusivity (400 times greater than that for Si at room temperature), allowing for high rate capability.[12] Finally, Ge-based anodes show isotropic lithiation behavior, while Si-based ones exhibit highly anisotropic behavior as well as nonhomogeneous alloying pathways for Li ions.[9] The phenomenon of isotropic lithiation may lead to Ge-based anodes exhibiting highly reversible capacities, as it minimizes fracturing in the anodes.

However, as is the case with Si-based anodes, a critical issue related to Ge-based anodes is that they exhibit a significant volume change (greater than 230%), which may lead to the cracking and pulverization of the Ge particles, resulting in poor cycling life.[11,13] To overcome this problem, numerous efforts have been made to design Ge-based materials that do not exhibit significant volume changes. These include reducing the particle size,[11] forming one-dimensional nanostructures,[9,14,15] dispersing Ge in an inactive/active matrix,[16] forming porous structures,[9,17] and coating shells with the Ge materials[18] in order to improve their electrochemical performances.

For example, Cho and co-workers have reported that the Li-ion storage ability of Ge nanoparticles depends on their morphology and changes when the particles are transformed from zero-dimensional hollow-type ones to three-dimensional porous assemblies.[18] They also demonstrated that Ge nanotubes and graphene-coated Ge nanowires exhibit high rate capabilities and long-term stable cyclability.[19] Further, Han and co-workers have proposed a simple method for synthesizing amorphous, porous, and hierarchically structured GeO_x anodes with a capacity as high as ~1250 mA h g^{-1} after 600 cycles.[20] Anodes of other Ge/carbon nanocomposites, including those with surface carbon coatings, also show significantly improved electrochemical performances as well as controlled volume expansion and stable cyclability over 100 cycles.[18,21−26] However, these materials are synthesized through complicated multistep processes that involve the use of expensive and hazardous organic-capped Ge precursors (*e.g.*, GeH_4 and $GeCl_4$).[27] In addition, magnesiothermic reduction involving the use of magnesium as a reducing agent can be dangerous owing to the large thermal shock generated during the chemical reaction.[16] Therefore, the development of a simple, safe, cost-effective, and scalable method for synthesizing high-performance Ge-based battery anodes is highly desired but still a challenge.

Herein, we present a simple and cost-effective technique for synthesizing mesoporous Ge particles. Metallic Zn, which has a low melting temperature (420 °C), is used as the reducing agent for the simple conversion of cheap GeO_2 into mesoporous Ge particles *via* a redox-transmetalation reaction[28] (*i.e.*, a zincothermic reduction reaction (ZRR)). This strategy has several advantages. To begin with, the reaction temperature for the ZRR is much lower than that for typical metallothermic reactions (*e.g.*, those involving Mg, Al, or Ca); hence, the shape of the original GeO_2 particles is preserved even after they have been converted into metallic Ge particles. Further, the large change in volume exhibited by the Ge particles during the lithiation/delithiation process is accommodated by the mesoporous structure of the particles. Finally, the ZRR process allows one to produce mesoporous Ge materials on a large scale through a one-step synthetic reaction using an environmentally benign and cost-effective approach. Using the ZRR process, it is possible to fabricate an optimized mesoporous Ge anode that exhibits a reversible capacity as high as ~1400 mAh g^{-1} after 300 cycles at a rate of 0.5 C (corresponding to the capacity retention of 99.5% compared to a capacity in the initial cycle), excellent rate capability, and stable cycling performance in a full cell containing the Ge anode and a $LiCoO_2$ cathode.

RESULTS AND DISCUSSION

A schematic illustration of the process for synthesizing mesoporous Ge materials *via* a redox-transmetalation reaction between Zn^0 and Ge^{4+} (GeO_2) is shown in Figure 1a. Hollow GeO_2 nanoparticles react with Zn vapor at a temperature well above the melting temperature of Zn metal, with Ge and ZnO forming after the ZRR. Subsequently, the byproduct ZnO is removed completely using hydrochloric acid, resulting in hollow mesoporous Ge nanoparticles. According to a previous study,[23] we synthesized hollow GeO_2 nanoparticles *via* the hydrolysis of Ge^{4+} and Sn^{4+} precursors (Ge^{4+}/Sn^{4+} molar ratio = 1:1) under basic conditions. This simultaneously generated insoluble GeO_2 and $Sn(OH)_4$ as white precipitates. The gradual dissolution of $Sn(OH)_4$ under basic conditions led to the formation of hollow GeO_2 nanoparticles. The surface morphology and microstructure of the as-synthesized GeO_2 nanoparticles were characterized using scanning electron microscopy (SEM) and transmission electron microscopy (TEM), as shown in Figure 1b. It was found that uniform ellipsoidal GeO_2 nanoparticles with sizes of 200−300 nm were synthesized; the void space within the particles was indicative of their hollow structure. The X-ray diffraction (XRD) pattern of the hollow GeO_2 particles suggested that the particles have a crystalline structure and are of trigonal GeO_2 (JCPDS card no. 36-1463) (Figure 1c). The resulting GeO_2 particles react with Zn metal *via* a ZRR process at a certain

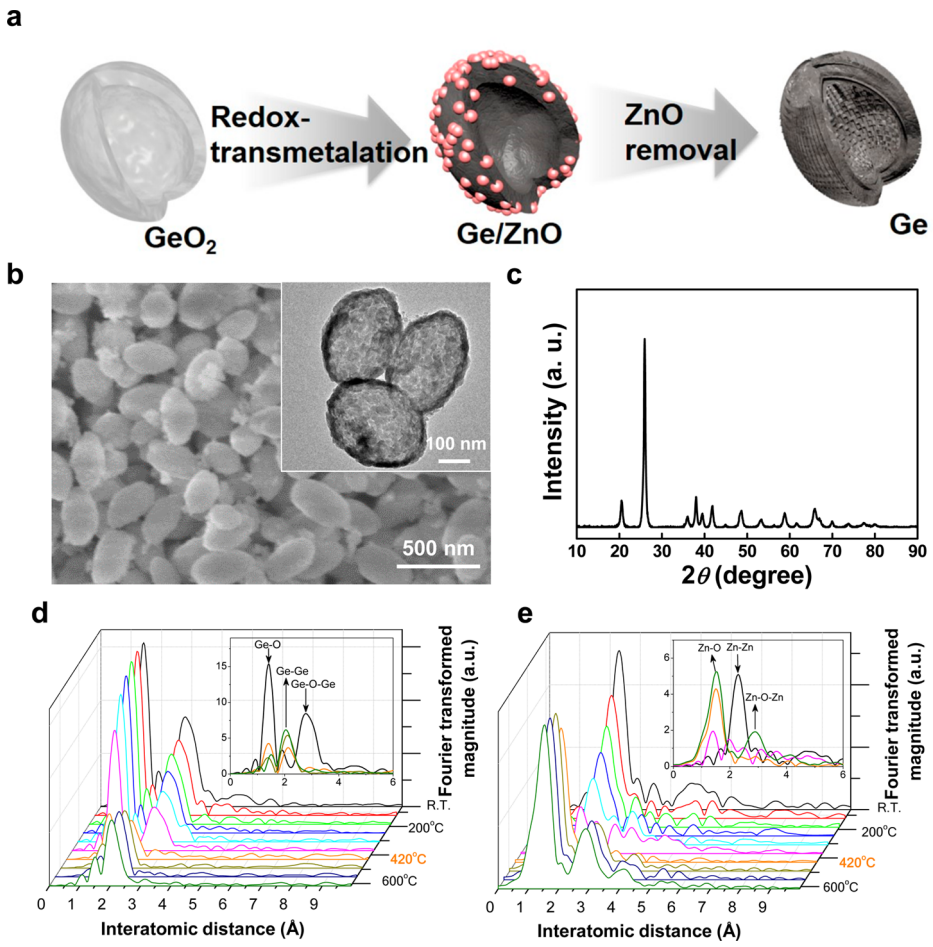

Figure 1. (a) Schematic illustration of the method for synthesizing mesoporous Ge materials *via* a unique redox-transmetalation process. (b) SEM images of the synthesized GeO_2 particles showing their ellipsoidal structure. Inset: HRTEM image of GeO_2 particles showing their hollow structure. (c) XRD pattern of the as-synthesized hollow GeO_2 particles. Radial distribution functions of (d) the Ge K-edge k^3 and (e) the Zn K-edge k^3-weighted XAFS spectra as functions of the temperature.

temperature range as the following chemical reaction:

$$GeO_2(s) + 2Zn(g) \rightarrow 2ZnO(s) + Ge(s)$$

$$\Delta G°(450\ °C) = -99.263\ kJmol^{-1} \quad (1)$$

that a redox-trans metalation process corresponding to $2Zn^0 + Ge^{4+} \rightarrow 2Zn^{2+} + Ge^0$ occurs was confirmed by temperature-dependent *in situ* X-ray absorption fine structure (XAFS) spectroscopy performed during the ZRR process. Because the spectroscopic method yields atomic-selective structural information related to the elements present, Ge and Zn K-edge XAFS measurements can elucidate the thermal dependence of the phase transition for every element on the ZRR.

The variations in the normalized Ge and Zn K-edge X-ray absorption near edge structure (XANES) spectra are shown in Supporting Information (Figure S1), while the corresponding radial distribution functions (RDFs) of the extended XAFS (EXAFS) spectra for temperatures of 25−600 °C (heating rate = 2.5 °C/min) are shown in Figure 1d,e. The spectral features corresponding to the oxide phase (GeO_2) and metallic Zn at room temperature change abruptly and simultaneously to those corresponding to metallic Ge and ZnO, respectively, at 420 °C. In particular, the Ge−O and Ge−O−Ge peaks of the oxide phase in the RDFs disappear and metallic Ge−Ge peaks are observed (Figure 1d), while the Zn−Zn metallic peak transforms into one corresponding to an oxide phase (ZnO) (Figure 1e). The fact that the XANES and EXAFS spectral features remain unchanged up to 600 °C indicates the successful formation of metallic Ge phase from GeO_2 through the redox-transmetalation process.

On the basis of the *in situ* XAFS spectroscopy results, we performed a ZRR reaction between hollow GeO_2 particles and Zn metal at several temperatures. A mixture of hollow GeO_2 nanoparticles and Zn (GeO_2/Zn weight ratio = 1:1.25) was heated at 390, 420, and 450 °C for 3 h and subsequently rinsed with 1 M HCl to dissolve the ZnO formed as byproduct. Next, the resulting products were characterized by XRD analysis (Figure 2c). The concentration of each component (*i.e.*, the Ge/GeO_2 ratio) was estimated from the areas under the XRD peaks (Figure 2d). Even at temperatures lower

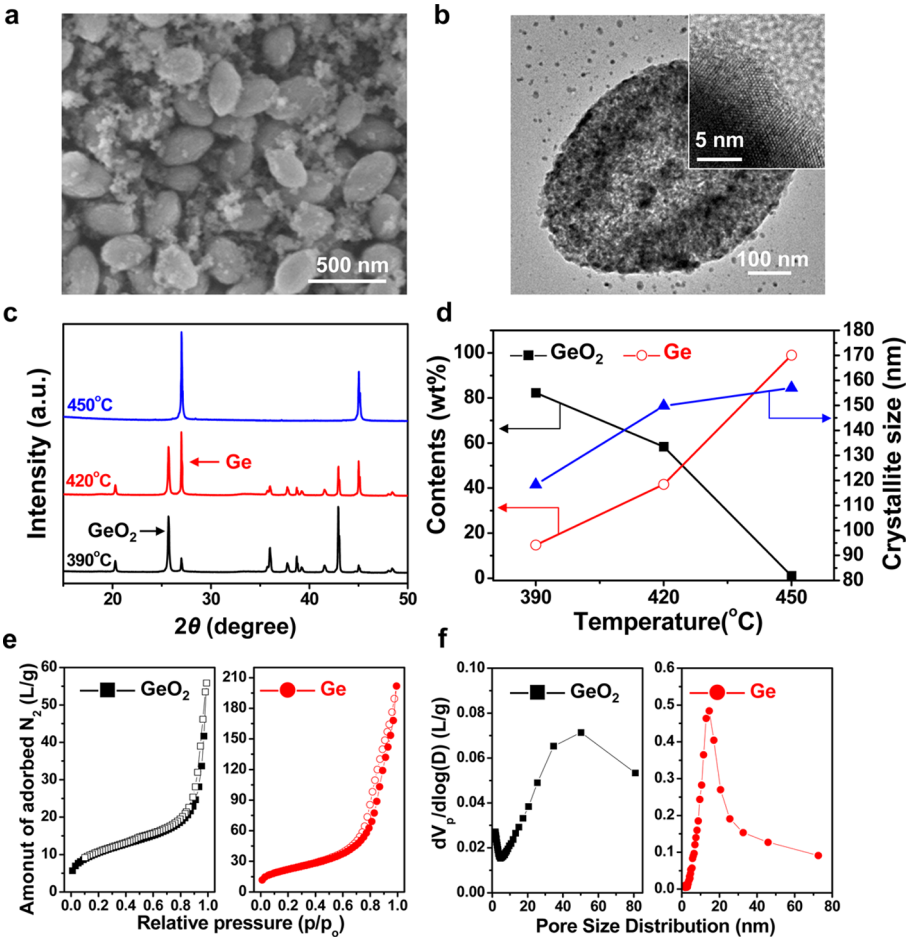

Figure 2. Characterization of hollow Ge particles synthesized by the ZRR process. (a) SEM image of shape-preserving mesoporous Ge particles with a hollow structure. (b) TEM image of the Ge particles showing the presence of mesopores. Inset: the crystalline structure of the Ge particles can be seen clearly. (c) XRD patterns of hollow Ge particles synthesized from hollow GeO_2 nanoparticles at three different reaction temperatures (390, 420, and 450 °C). (d) Concentration and crystallite size of Ge, as estimated from the XRD pattern shown in (c). (e) Nitrogen adsorption–desorption plots and (f) pore size distribution plots of the hollow GeO_2 and mesoporous Ge ellipsoidal particles obtained by the ZRR process at 450 °C.

than the melting temperature of Zn, a small amount of Ge (14.7%) was produced, owing to the exothermal heat generated during the ZRR process (see bottom of Figure 2c). When the reaction temperature reached the melting temperature of Zn (420 °C), Ge was formed in a greater amount (41.6%), indicating that a larger portion of GeO_2 was transformed into Ge (see middle of Figure 2c). With a further increase in the reaction temperature to 450 °C, all of the GeO_2 was completely converted into pure metallic Ge (see top of Figure 2c). The ZRR (at 450 °C) of the hollow GeO_2 nanoparticles led to the formation of shape-preserving mesoporous Ge nanoparticles without there being a significant change in the dimensions of the nanoparticles (SEM image in Figure 2a) or a change in the original hollow structure of the GeO_2 nanoparticles (TEM image in Figure 2b). Further, high-resolution TEM confirmed that highly crystalline Ge was obtained after the ZRR process (inset of Figure 2b).

The crystallite sizes of the Ge nanoparticles formed at different temperatures were calculated using the Scherrer formula and the XRD data.[29] The average size of the crystalline domains was calculated using the following formula:

$$\tau = K\lambda/\beta \cos\theta \qquad (2)$$

where K is a dimensionless shape factor, λ is the X-ray wavelength, β is the degree of line broadening at half the maximum intensity, and θ is the Bragg angle. It was found that the crystallite sizes of the Ge particles synthesized at 390, 420, and 450 °C were 118, 149, and 157 nm, respectively. With an increase in the ZRR temperature, the size of the Ge crystals increased significantly (Figure 2d). A Brunauer–Emmett–Teller (BET) analysis indicated that the hollow GeO_2 nanoparticles had a BET surface area of 37.84 $m^2\ g^{-1}$, while the hollow Ge nanoparticles had a BET surface area of 80 $m^2\ g^{-1}$ (Figure 2e), indicating that a number of mesopores were formed during the ZRR process. The pore size distribution, obtained using the Barrett–Joyner–Halenda (BJH) method, suggested that the hollow Ge nanoparticles had a narrower pore size

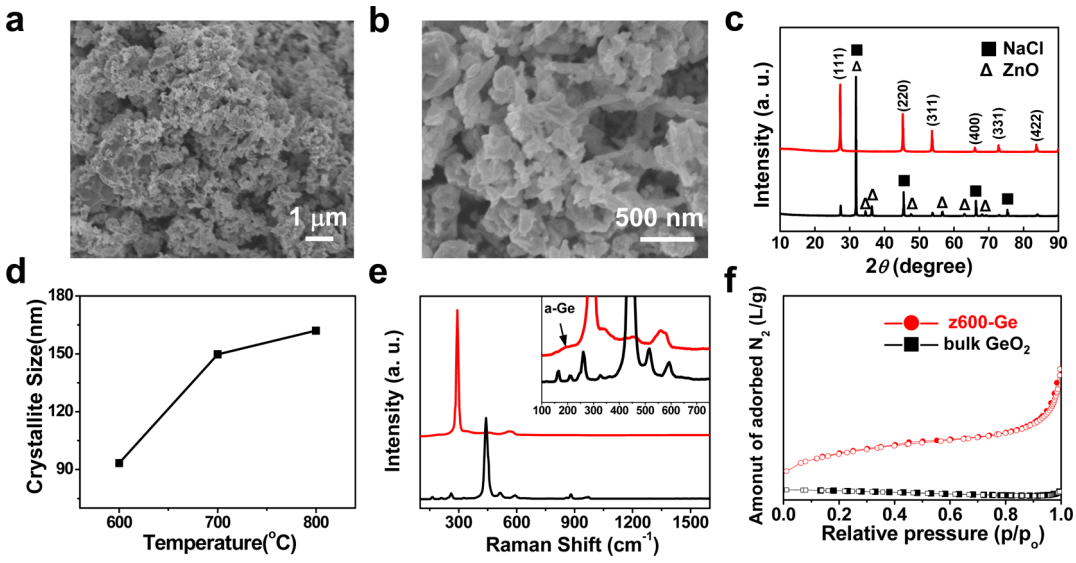

Figure 3. Characterization of the mesoporous Ge particles synthesized from bulk GeO_2 by the ZRR process at 600 °C. (a) Low-magnification and (b) high-magnification SEM images of the as-synthesized z600-Ge. (c) XRD pattern of the sample obtained immediately after the ZRR process (bottom) and that of the HCl-treated sample (top). (d) Crystallite sizes of the zGe samples obtained at three different temperatures. (e) Raman spectra of the z600-Ge particles (red line) and bulk GeO_2 (black line). Inset: indicates that the z600-Ge particles contained both crystalline Ge and amorphous Ge. (f) Nitrogen adsorption−desorption plots of bulk GeO_2 and the z600-Ge particles.

distribution (smaller than 20 nm in diameter) than that of the hollow GeO_2 nanoparticles, which ranged from 10 to 80 nm in diameter (Figure 2f).

However, these nanomaterials have several disadvantages, which include (i) high cost to synthesize due to the complexity of their synthesis processes, (ii) the low volumetric energy density resulting from the lowered tap density of the nanoparticles, and (iii) undesired side reactions between the electrode and electrolyte owing to the large surface areas.[4]

In addition to synthesizing Ge nanomaterials, we employed the ZRR process to fabricate micrometer-sized bulk GeO_2 particles. SEM images of commercially available bulk GeO_2 particles show large secondary particles (10−20 μm), which formed by the irregular stacking of primary particles (200−500 nm). Further, tiny pores are formed in the stacked regions of the primary particles (Supporting Information, Figures S2a and S2b). The XRD pattern of the GeO_2 particles indicates a crystalline structure consisting of a trigonal GeO_2 phase (Supporting Information, Figure S2c).[30] The ZRR process for synthesizing metallic Ge from bulk GeO_2 particles with a low surface area requires additional heat. When the bulk GeO_2 reacted with Zn vapor at 550 °C for 3 h, most of the GeO_2 was converted into Ge; however, a small amount of GeO_2 remained (Supporting Information, Figure S3). It should be noted that the GeO_2 particles, which were initially composed of a trigonal phase, transformed such that they consisted of a tetragonal phase (JCPDS card no. 35-0729), owing to the additional heat generated during the ZRR process.

When the bulk GeO_2 particles were reacted with Zn vapor in the presence of NaCl (employed as a heat scavenger) at 600 °C for 3 h in an argon atmosphere, they resulted in pure Ge particles (z600-Ge) and ZnO (byproduct), with no unreacted GeO_2 being present, as confirmed by the XRD pattern (Figure 3c). During the ZRR process, the secondary GeO_2 particles broke into numerous submicron-sized primary particles and were simultaneously converted into submicron-sized Ge particles. Figure 3a,b show SEM images of the z600-Ge particles of 200−500 nm in size. In general, metallothermic reduction processes generate large amounts of heat, resulting in the collapse of original structure of the metal oxide material.[31,32] To solve this problem, we employed NaCl as a heat scavenger to preserve the original structure of the GeO_2 particles after the ZRR process. Powders of GeO_2, NaCl, and Zn (GeO_2/Zn/NaCl = 1:1.25:2.25 by mass) were mixed homogeneously in an argon-filled glovebox. After the completion of the chemical reduction process, the NaCl was removed by washing the product several times with deionized water, while the ZnO formed as a byproduct was removed with HCl. The XRD pattern of the as-synthesized Ge/ZnO composite indicated that it contained a large amount of ZnO (as a byproduct) and the NaCl salt used as a heat scavenger (see bottom of Figure 3c). When the composite material was dissolved in a 1 M HCl solution, the ZnO was completely removed, as indicated by the XRD pattern shown in Figure 3c (see top). After the complete removal of ZnO and NaCl, the XRD pattern of the z600-Ge particles suggested that the particles had a crystalline structure of diamond cubic Ge (JCPDS card no. 04-0545).

Meanwhile, when the ZRR temperature of the bulk GeO_2 was increased to 700 and 800 °C, a mixture of

mesoporous/macroporous particles and micrometer-sized aggregated porous Ge particles were synthesized, respectively, owing to the excessive exothermic heat generated (Supporting Information, Figure S4). Using the Scherrer formula, the crystallite sizes of the Ge particles synthesized at 600, 700, and 800 were found to be 93, 149, and 162 nm, respectively. With an increase in the reduction temperature, the size of the Ge particles increased significantly (Figure 3d). Thus, the reaction temperature affects both the particle size and the crystallite size. Raman spectroscopy is another tool that can yield information on the intrinsic characteristics of GeO_2 and metallic Ge. Figure 3e shows the Raman spectra of z600-Ge and bulk GeO_2. The spectrum of the bulk GeO_2 powder shows a strong peak at 448 cm^{-1}, which corresponds to symmetric Ge−O−Ge stretching, while the bands at 167 and 260 cm^{-1} correspond to the complex translation and rotation of the GeO_4 tetrahedra (see bottom of Figure 3e).[15] In the Raman spectrum of z600-Ge, two peaks, corresponding to crystalline and amorphous Ge, are observed at 300 and 270 cm^{-1}, respectively (inset of Figure 3e).[27] In addition, nitrogen adsorption BET measurements indicated that the specific surface area of commercially available bulk GeO_2 is very low (0.01 $m^2\ g^{-1}$), while that of z600-Ge is significantly higher (~15 $m^2\ g^{-1}$), owing to the formation of mesopores during the ZRR process (Figure 3f).

The galvanostatic discharge−charge cycling of the zGe particles was performed for potentials of 0.005−1.5 V at different current densities. Commercially available anodes containing micrometer-sized Ge particles showed a remarkably high initial Coulombic efficiency of 93.3%, owing to the good electrical conductivity of single-crystalline Ge (Supporting Information, Figure S5).[14] However, an electrode of bulk Ge exhibited a capacity retention rate as low as 17.5% at a 0.2 C rate after 100 cycles; this was because of the large volume change experienced by the Ge particles during battery operation.[14] In contrast, an electrode of the hollow Ge nanoparticles obtained by the ZRR process at 450 °C (seen in Figure 2) showed high cycling stability, exhibiting outstanding capacity retention (91.4%) at 0.5 C after 200 cycles (Figure 4b). This is attributed to the peculiar structure of the anode, which had mesopores in the shell part and nanocavities in the interior; these can provide extra void space and accommodate the large volume changes occurring during the lithiation/delithiation process. However, the initial Coulombic efficiency of the anode of mesoporous and hollow Ge particles was 74%, which corresponded to a discharge (lithiation) capacity of 1470 mA h g^{-1} and a charge (delithiation) capacity of 1086 mA h g^{-1} (Figure 4a). This was due to a side reaction of the nanoparticles, which had a high surface area.

Given the various advantages and disadvantages of nanomaterials, the z600-Ge particles, which had a lower surface area and a higher crystallinity than those of hollow Ge particles, may be more suitable anodic materials for LIBs. Figure 4c shows the first cycle voltage profile corresponding to the discharge and charge of the z600-Ge electrodes at a rate of 0.05 C when used in a coin-type half-cell. The first discharge and charge capacities of the z600-Ge electrode were 1585 and 1410 mA h g^{-1}, respectively; these corresponded to an initial Coulombic efficiency of 89%. It should be noted that an increase in the ZRR temperature leads to an increase in the initial Coulombic efficiency. This suggests that increasing the crystallite and particle sizes of Ge increases its electrical conductivity, resulting in an increase in the kinetics of lithiation and delithiation. The Ge-based electrodes (z700-Ge and z800-Ge) obtained by the ZRR process at 700 and 800 °C showed markedly improved initial Coulombic efficiencies of 90 and 92.2%, respectively (Supporting Information, Figure S6a and S6c). However, as expected, the cycling performances of both the electrodes (z700-Ge and z800-Ge) resulted in significant capacity fading because of the large volume changes occurring owing to the increase in particle size. The z700-Ge and z800-Ge anodes showed capacity retention rates of 59% and 17%, respectively, at a rate of 0.2 C after 100 cycles (Supporting Information, Figures S6b and S6d). In contrast, the z600-Ge electrode exhibited outstanding long-term cycling stability, exhibiting a capacity retention rate of more than 99.5% at 0.5 C rate after 300 cycles (Figure 4d). Furthermore, the Coulombic efficiency per cycle was more than 99.5%, demonstrating that the mesopores act as effective active sites for reversible electrochemical lithium storage.

The excellent electrochemical performances of the z-Ge series of electrodes can be explained as follows: (i) the crystallite size of the Ge particles depends on the ZRR temperature and affects the initial Coulombic efficiency, (ii) decreasing the crystallite size improves the cycling stability, as increasing the amorphous content within the Ge particles improves their electrochemical properties while also preventing particle fracturing and decreasing the volume change experienced during cycling,[33] and (iii) when mesopores are present within an active material in a suitable number density, they can act as buffer spaces and accommodate the large volume changes experienced during the repeated cycling.

As a control experiment, we synthesized macroporous Ge particles using a well-known metallothermic reduction reaction, namely a magnesiothermic reaction, which was performed at 700 °C for 1 h. Bulk GeO_2 was successfully converted into Ge particles (denoted as m-Ge) and MgO (byproduct) (GeO_2 (s) + 2Mg (g) → 2MgO (s) + Ge(s), $\Delta G°(700\ °C) = -599.63$ kJ mol^{-1}). However, significantly aggregated Ge particles were obtained, owing to the large amount of heat generated during the chemical reduction process (Supporting

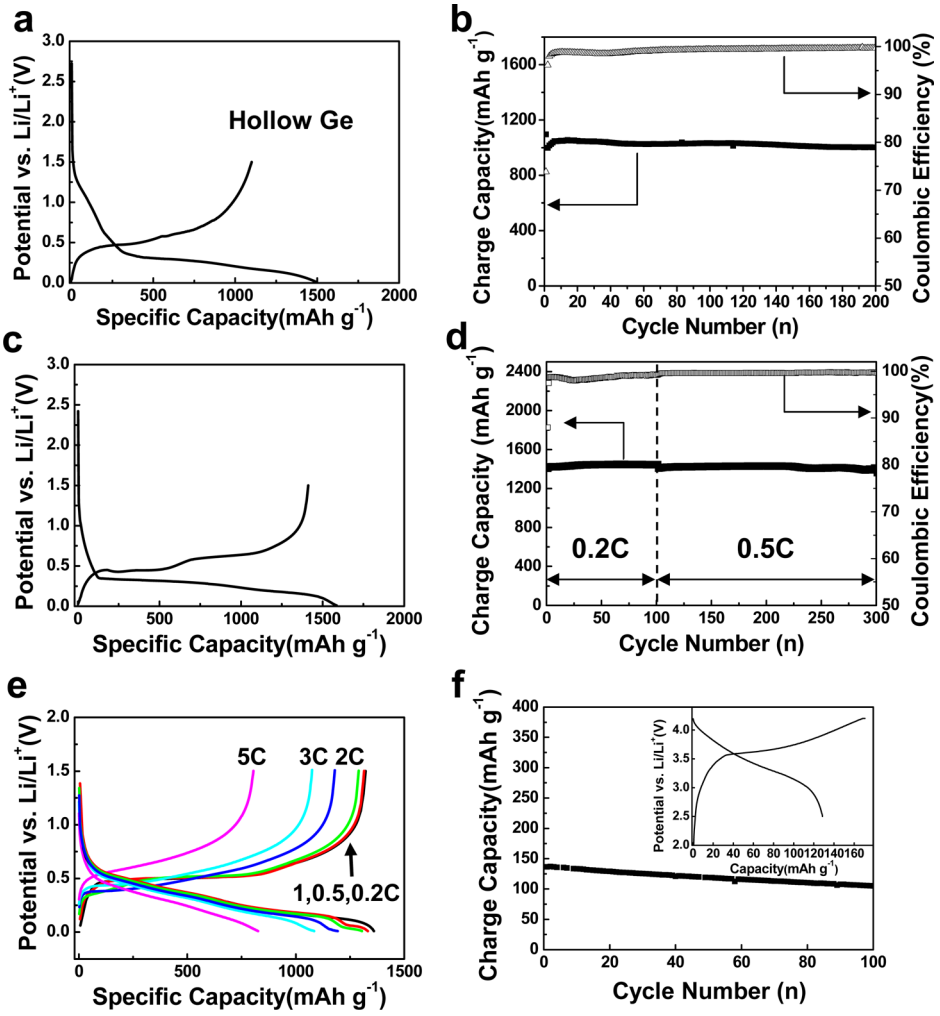

Figure 4. Electrochemical performances of the electrodes formed using the hollow Ge and z600-Ge particles. (a) First-cycle voltage profile of the hollow Ge particles-based electrode obtained at a rate of 0.05 C in the range of 0.005−1.5 V. (b) Cycling performance of the hollow Ge particles-based electrode obtained at a rate of 0.2 C. (c) First-cycle voltage profile of the z600-Ge electrode at 0.05 C in the range of 0.005−1.5 V. (d) Cycling performances of the z-600Ge electrode at 0.2 C (1st to 100th cycles) and 0.5 C (101th to 300th cycles). (e) Rate capabilities of the z600-Ge electrode at the same charge/discharge rates. (f) Cycling performance of a full cell ($LiCoO_2$ cathode and z600-Ge anode) at 0.5 C in the range of 2.5−4.2 V. Inset: first-cycle voltage profile of the full cell.

Information, Figure S7a). An electrode of m-Ge showed an initial Coulombic efficiency of 81.9% (Supporting Information, Figure S7c). In addition, the m-Ge electrode exhibited a gradual decay in capacity during cycling, showing a capacity retention rate of 73.7% at a rate of 0.2 C after 100 cycles; this was due to the large volume change experienced by the aggregated Ge particles (Supporting Information, Figure S7d).

Moreover, the z600-Ge electrode exhibited specific capacities of 1178, 1075, and 804 mA h g^{-1} at current densities of 2.63 (2 C), 3.89 (3 C), and 6.47 A g^{-1} (5 C), respectively, even though no coating layer (such as that of carbon, metal, or conductive polymers)[34−38] was introduced on the Ge surface (Figure 4e). The electrochemical performances of the anodes of the mesoporous Ge nanoparticles were tested in half cells. However, this is not sufficient to determine the suitability of the nanomaterials as anodic materials for LIBs. Thus, we employed a full cell (loading density of ∼1 mA h cm^{-2}), in which a z600-Ge electrode was coupled with a $LiCoO_2$ cathode. The first charge/discharge voltage profile of the Ge/$LiCoO_2$ full cell shows that it had a Coulombic efficiency of 80% during precycling at a rate of 0.1 C for voltages of 2.5−4.2 V (see inset of Figure 4f). During subsequent long-term cycling (including a second cycle of charging/discharging, which was performed at 0.5 C), the anode exhibited a capacity retention rate of ∼80% after 100 cycles (Figure 4f). This demonstrates that the mesoporous z600-Ge is a promising anodic material for practical LIBs.

Electrodes of mesoporous Ge (fabricated by a ZRR process) showed high specific capacities, outstanding cycling stabilities, and excellent rate capabilities. However, the other critical issue determining the suitability of an anodic material for use in LIBs is whether a stable solid-electrolyte interphase (SEI) layer is formed on

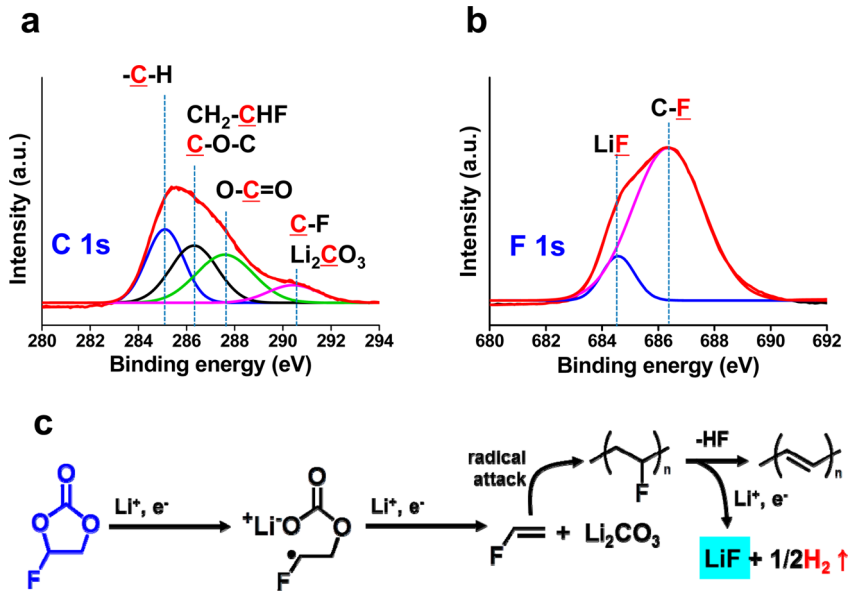

Figure 5. (a) C 1s and F 1s XPS spectra of the mesoporous z-Ge electrode after 300 cycles. (c) Reaction mechanism showing the formation of the C—F bond and LiF.[39]

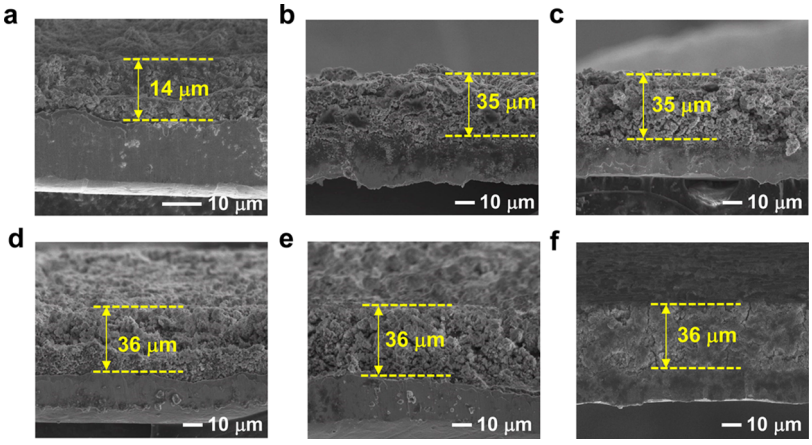

Figure 6. Cross-sectional SEM images of the z600-Ge electrode (a) before and after (b) the 1st cycle, (c) 5th cycle, (d) 10th cycle, (e) 20th cycle, and (f) 300th cycle.

the electrode surface during repeated lithiation/delithiation.[39]

It is should be noted that the surface chemistry of metal-based electrodes with high theoretical capacities is a critically important issue that influences the lithiation/delithiation kinetics and the interfacial stability of the electrodes during long-term cycling. To investigate the surface chemistry of the Ge electrodes, *ex situ* X-ray photoelectron spectroscopy (XPS) analyses were performed. Figure 5 shows the F 1s and C 1s XPS spectra of a Ge electrode after 300 cycles. Two major peaks were seen in the F 1s XPS spectrum (Figure 5b): one was assignable to the C—F bond (686.3 eV) produced by the decomposition of fluoroethylene carbonate (FEC) (FEC + Li^+ + e^- → CH_2═CHF + Li_2CO_3, CH_2═CHF → C—F containing polymer species),[39] and the other was attributable to LiF (684.5 eV) formed by the reaction of the C—F-containing polymer species $(CH_2—CHF)_n$ with Li^+ ions and electrons, as described in Figure 5c. This demonstrates that employing FEC as an additive is an efficient means of forming an SEI layer on Ge electrodes and thus preventing unwanted electrolyte decomposition during cycling. The C 1s XPS spectrum shows peaks corresponding to four types of carbon: C—H (285.0 eV), C—O—C/CH_2—CHF (286.5 eV), O—C═O (carbonate species; 288.0 eV), and Li_2CO_3/C—F (290.5 eV) (Figure 5a). The appearance of two peaks corresponding to carbon bonded to fluorine (C—F and CH_2—CHF), at 286.5 and 290.5 eV, respectively,[40] confirms that FEC acts as an SEI-forming agent on the z600-Ge electrode during long-term cycling.

More interestingly, when we investigated the swelling of the z600-Ge electrodes after repeated cycles, we found that the electrode thickness increased significantly by up to 150% during the first cycle, owing to the formation of lithium-alloying products (Figure 6b).

However, during subsequent long-term cycling (*i.e.*, until the 300th cycle), the electrode thickness is quite similar to that after the first cycle (Figures 6c–f), increasing to 157% of the original value. This result once again demonstrates that the stable SEI layer on the z600-Ge electrode surface forms and the mesoporous structure of z600-Ge mitigates the large volume change occurring during long-term cycling, resulting in highly stable cycling performance. In contrast, commercial Ge electrode showed a remarkable increase of electrode thickness as a function of cycles. After 300 cycles, the electrode swelling of >350% was observed (Supporting Information, Figure S8).

CONCLUSION

In summary, we demonstrated a simple and cost-effective large-scale process for synthesizing mesoporous Ge particles *via* a unique redox-transmetalation reaction between GeO_2 and Zn powders. Using *in situ* XAFS analyses performed at various temperatures, the redox-transmetalation reaction was monitored. This method allowed us to preserve the shape of the original GeO_2 particles and to form additional mesopores in the resulting Ge particles. There are several other advantages of this technique. The low-temperature reduction process enabled us to synthesize metallic particles from inexpensive metal oxides on a large scale. Next, the resulting mesoporous Ge particles exhibited outstanding electrochemical properties when used as anode materials in LIBs, showing a specific capacity as high as ~1400 mA h g^{-1}, highly stable cycling performance (capacity retention rate of 99.5% after 300 cycles), and excellent rate capability (a specific capacity of 804 mA h g^{-1} at a rate of 5 C). This simple strategy may open up an effective way for synthesizing mesoporous particles of other metals *via* a one-step synthetic reaction through an environmentally benign and cost-effective approach.

METHODS

Synthesis of Hollow Germanium Oxide Materials. Hollow GeO_2 particles were synthesized by the hydrolysis of $GeCl_4$ and $SnCl_4$ (Ge/Sn molar ratio = 1:1) under ultrasonication. First, 1.635 g of $SnCl_4 \cdot 5H_2O$ was dissolved in 35 mL of ethanol (99.9%, Sigma-Aldrich) under ultrasonication for 10 min. Next, 1 g of $GeCl_4$ (99.999%, Alfa Aesar) dissolved in 10 mL of ethanol was added to the $SnCl_4$ solution. Subsequently, 7 mL of deionized water and 1 mL of concentrated NH_4OH were added to the above mixture and the mixture was subjected to ultrasonication for 120 min. The resulting white precipitate was collected by centrifugation (3500 rpm for 10 min) and rinsed several times with ethanol before being dried in vacuum at 80 °C.

Synthesis of Mesoporous Germanium Materials. Commercially available GeO_2 (99.999%, Sigma-Aldrich) was mixed uniformly with a zinc powder (Zn 99.9%, Alfa Aesar) in a mortar. The mixture was placed in a stainless steel vessel, whose cap was then closed in an argon-filled glovebox. In a typical process, the furnace was heated to 390–800 °C at a rate of 5 °C min^{-1} and kept at the target temperature for 3 h. The thus-obtained samples were immersed in a 1 M HCl solution at 30 °C for 1 h to remove the ZnO formed as a byproduct. From this synthetic process, Ge particles of >65% were obtained in one batch.

Physical Characterization. The surface morphologies of the GeO_2 and Ge particles were characterized using field-emission scanning electron microscopy (FESEM, Hitachi S-4800), which was performed at 10 kV. The microstructures of the GeO_2 particles and the as-synthesized Ge particles were investigated using XRD analyses (Bruker D8-Advance), which were performed at 3 kW using Cu Kα radiation. The Raman spectra to characterize the Ge phase in the Ge and GeO_2 particles were obtained using a JASCO spectrometer (NRS-3000), which was operated at 532 nm.

X-ray Absorption Spectroscopy. The temperature-dependent *in situ* Ge and Zn K-edge X-ray absorption spectra of the mixture of the Ge and Zn particles were collected at the BL10C beamline of the Pohang light source (PLS-II) in the top-up mode under a ring current of 300 mA at 3.0 GeV. The XANES and EXAFS analyses were also performed under the same conditions. A monochromatic X-ray beam was obtained from high-intensity X-ray photons emitted by a multiple wiggler source using a liquid-nitrogen-cooled Si (111) double crystal monochromator (Bruker ASC). The transmitted XAFS spectra were collected using a laboratory-made heating stage for temperatures ranging from the room temperature to 600 °C for ~4 h (heating rate = 2.5 °C/min).

Electrochemical Test. The electrochemical properties of the Ge-based electrodes were evaluated using coin-type half cells (2016R) at 25 °C. The Ge-based electrodes were composed of the Ge active material, super-P carbon black, and poly(acrylic acid)/sodium carboxymethyl cellulose (1:1, w/w) as binder in a weight ratio of 7:1.5:1.5. The electrolyte used was 1.3 M $LiPF_6$ containing ethylene carbonate/diethyl carbonate (PANAX Starlyte, Korea, 3/7 (v/v)) and 10 wt % fluoroethylene carbonate as an additive. The half cells were tested galvanostatically between 0.005 and 1.5 V (versus Li/Li^+) for C rates of 0.05–7 C. The coin-type full cells consisted of an anode of the synthesized material (z600-Ge) and a $LiCoO_2$ cathode. The cell performance was examined using a cycle tester (WBCS 3000 battery systems, Wonatech). The full cells were cycled at rates of 0.1–0.5 C between 2.5 and 4.2 V.

Conflict of Interest: The authors declare no competing financial interest.

Supporting Information Available: Normalized K-edge XANES spectra of Ge and Zn as functions of the temperature during a redox-transmetalation process; characterization of mesoporous Ge particles synthesized by zincothermic reaction and their electrochemical tests. This material is available free of charge *via* the Internet at http://pubs.acs.org.

Acknowledgment. This work was supported by the IT R&D program of MOTIE/KEIT (10046309).

REFERENCES AND NOTES

1. Nazri, G.-A.; Pistoia, G. *Lithium Batteries: Science and Technology*; Kluwer Academic/Plenum: New York, 2004.
2. Tarascon, J. M.; Armand, M. Issues and Challenges Facing Rechargeable Lithium Batteries. *Nature* **2001**, *414*, 359–367.
3. Ozawa, K. *Lithium Ion Rechargeable Batteries*. Wiley: New York, 2009.
4. Song, M.-K.; Park, S.; Alamgir, F. M.; Cho, J.; Liu, M. Nanostructured Electrodes for Lithium-Ion and Lithium-Air Batteries: The Latest Developments, Challenges, and Perspectives. *Mater. Sci. Eng., R* **2011**, *72*, 203–252.
5. Choi, N.-S.; Chen, Z.; Freunberger, S. A.; Ji, X.; Sun, Y.-K.; Amine, K.; Yushin, G.; Nazar, L. F.; Cho, J.; Bruce, P. G. Challenges Facing Lithium Batteries and Electrical Double-Layer Capacitors. *Angew. Chem., Int. Ed.* **2012**, *51*, 9994–10024.

6. Chockla, A. M.; Klavetter, K. C.; Mullins, C. B.; Korgel, B. A. Solution-Grown Germanium Nanowire Anodes for Lithium-Ion Batteries. *ACS Appl. Mater. Interface* **2012**, *4*, 4658–4664.
7. Yuan, F.-W.; Tuan, H.-Y. Scalable Solution-Grown High-Germanium-Nanoparticle-Loading Graphene Nanocomposites as High-Performance Lithium-Ion Battery Electrodes: An Example of a Graphene-Based Platform toward Practical Full-Cell Applications. *Chem. Mater.* **2014**, *26*, 2172–2179.
8. Graetz, J.; Ahn, C. C.; Yazami, R.; Fultz, B. Nanocrystalline and Thin Film Germanium Electrodes with High Lithium Capacity and High Rate Capabilities. *J. Electrochem. Soc.* **2004**, *151*, A698–A702.
9. Liu, X. H.; Huang, S.; Picraux, S. T.; Li, J.; Zhu, T.; Huang, J. Y. Reversible Nanopore Formation in Ge Nanowires during Lithiation–Delithiation Cycling: An In Situ Transmission Electron Microscopy Study. *Nano Lett.* **2011**, *11*, 3991–3997.
10. Wang, D.; Chang, Y.-L.; Wang, Q.; Cao, J.; Farmer, D.; Gordon, R.; Dai, H. Surface Chemistry and Electrical Properties of Germanium Nanowires. *J. Am. Chem. Soc.* **2004**, *126*, 11602–11611.
11. Fuller, C. S.; Severiens, J. C. Mobility of Impurity Ions in Germanium and Silicon. *Phys. Rev.* **1954**, *96*, 21–24.
12. Liang, W.; Yang, H.; Fan, F.; Liu, Y.; Liu, X. H.; Huang, J. Y.; Zhu, T.; Zhang, S. Tough Germanium Nanoparticles under Electrochemical Cycling. *ACS Nano* **2013**, *7*, 3427–3433.
13. Seo, M.-H.; Park, M.; Lee, K. T.; Kim, K.; Kim, J.; Cho, J. High Performance Ge Nanowire Anode Sheathed with Carbon for Lithium Rechargeable Batteries. *Energy Environ. Sci.* **2011**, *4*, 425–428.
14. Chan, C. K.; Zhang, X. F.; Cui, Y. High Capacity Li Ion Battery Anodes Using Ge Nanowires. *Nano Lett.* **2008**, *8*, 307–309.
15. Seng, K. H.; Park, M.-H.; Guo, Z. P.; Liu, H. K.; Cho, J. Catalytic Role of Ge in Highly Reversible GeO_2/Ge/C Nanocomposite Anode Material for Lithium Batteries. *Nano Lett.* **2013**, *13*, 1230–1236.
16. Yang, L. C.; Gao, Q. S.; Li, L.; Tang, Y.; Wu, Y. P. Mesoporous Germanium as Anode Material of High Capacity and Good Cycling Prepared by a Mechanochemical Reaction. *Electrochem. Commun.* **2010**, *12*, 418–421.
17. Xue, D. J.; Xin, S.; Yan, Y.; Jiang, K. C.; Yin, Y. X.; Guo, Y. G.; Wan, L. J. Improving the Electrode Performance of Ge through Ge@C Core–Shell Nanoparticles and Graphene Networks. *J. Am. Chem. Soc.* **2012**, *134*, 2512–2515.
18. Kim, H.; Son, Y.; Park, C.; Cho, J.; Choi, H. C. Catalyst-Free Direct Growth of a Single to A Few Layers of Graphene on a Germanium Nanowire for the Anode Material of a Lithium Battery. *Angew. Chem., Int. Ed.* **2013**, *52*, 5997–6001.
19. Park, M. H.; Kim, K.; Kim, J.; Cho, J. Flexible Dimensional Control of High-Capacity Li-Ion Battery Anodes: From 0D Hollow to 3D Porous Germanium Nanoparticle Assemblies. *Adv. Mater.* **2010**, *22*, 415–418.
20. Wang, X. L.; Han, W. Q.; Chen, H.; Bai, J.; Tyson, T. A.; Yu, X. Q.; Wang, X. J.; Yang, X. Q. Amorphous Hierarchical Porous GeO(*x*) as High-Capacity Anodes for Li Ion Batteries with Very Long Cycling Life. *J. Am. Chem. Soc.* **2011**, *133*, 20692–20695.
21. Li, S.; Chen, C.; Fu, K.; White, R.; Zhao, C.; Bradford, P. D.; Zhang, X. Nanosized Ge@CNF, Ge@C@CNF and Ge@CNF@C Composites *via* Chemical Vapour Deposition Method for Use in Advanced Lithium-Ion Batteries. *J. Power Sources* **2014**, *253*, 366–372.
22. Wei, W.; Guo, L. One-Step In Situ Synthesis of GeO_2/Graphene Composites Anode for High-Performance Li-Ion Batteries. *Part. Part. Syst. Charact.* **2013**, *30*, 658–661.
23. Li, L.; Seng, K. H.; Feng, C.; Liu, H. K.; Guo, Z. Synthesis of Hollow GeO_2 Nanostructures, Transformation into Ge@C, and Lithium Storage Properties. *J. Mater. Chem. A* **2013**, *1*, 7666–7672.
24. Li, D.; Seng, K. H.; Shi, D.; Chen, Z.; Liu, H. K.; Guo, Z. A Unique Sandwich-Structured C/Ge/Graphene Nanocomposite as an Anode Material for High Power Lithium Ion Batteries. *J. Mater. Chem. A* **2013**, *1*, 14115–14121.
25. Seng, K. H.; Park, M. H.; Guo, Z. P.; Liu, H. K.; Cho, J. Self-Assembled Germanium/Carbon Nanostructures as High-Power Anode Material for the Lithium-Ion Battery. *Angew. Chem., Int. Ed.* **2012**, *51*, 5657–5661.
26. Vaughn, D. D., II; Schaak, R. E. Synthesis, Properties and Applications of Colloidal Germanium and Germanium-Based Nanomaterials. *Chem. Soc. Rev.* **2013**, *42*, 2861–2879.
27. Chiasera, A.; Macchi, C.; Mariazzi, S.; Valligatla, S.; Lunelli, L.; Pederzolli, C.; Rao, D. N.; Somoza, A.; Brusa, R. S.; Ferrari, M. CO_2 Laser Irradiation of GeO_2 Planar Waveguide Fabricated by RF-Sputtering. *Opt. Mater. Express* **2013**, *3*, 1561–1570.
28. Lee, W.-R.; Kim, M. G.; Choi, J. R.; Park, J. I.; Ko, S. J.; Oh, S. J.; Cheon, J. Redox-Transmetalation Process as a Generalized Synthetic Strategy for Core–Shell Magnetic Nanoparticles. *J. Am. Chem. Soc.* **2005**, *127*, 16090–16097.
29. Cullity, B. D. *Elements of X-Ray Diffraction*; Addison-Wesley: Edinburgh, UK. 1978.
30. Smith, G. S.; Isaacs, P. B. The Crystal Structure of Quartz-like GeO_2. *Acta Crystallogr.* **1964**, *17*, 842–846.
31. Won, C. W.; Nersisyan, H. H.; Won, H. I.; Lee, J. H. Refractory Metal Nanopowders: Synthesis and Characterization. *Curr. Opin. Solid State Mater. Sci.* **2010**, *14*, 53–68.
32. Luo, W.; Wang, X.; Meyers, C.; Wannenmacher, N.; Sirisaksoontorn, W.; Lerner, M. M.; Ji, X. Efficient Fabrication of Nanoporous Si and Si/Ge Enabled by a Heat Scavenger in Magnesiothermic Reactions. *Sci. Rep.* **2013**, *3*, 2222.
33. Cui, L.-F.; Ruffo, R.; Chan, C. K.; Peng, H.; Cui, Y. Crystalline-Amorphous Core–Shell Silicon Nanowires for High Capacity and High Current Battery Electrodes. *Nano Lett.* **2008**, *9*, 491–495.
34. Yu, Y.; Gu, L.; Zhu, C.; Tsukimoto, S.; van Aken, P. A.; Maier, J. Reversible Storage of Lithium in Silver-Coated Three-Dimensional Macroporous Silicon. *Adv. Mater.* **2010**, *22*, 2247–2250.
35. Yoo, H.; Lee, J.-I.; Kim, H.; Lee, J.-P.; Cho, J.; Park, S. Helical Silicon/Silicon Oxide Core–Shell Anodes Grown onto the Surface of Bulk Silicon. *Nano Lett.* **2011**, *11*, 4324–4328.
36. Wu, H.; Chan, G.; Choi, J. W.; Ryu, I.; Yao, Y.; McDowell, M. T.; Lee, S. W.; Jackson, A.; Yang, Y.; Hu, L.; *et al.* Stable Cycling of Double-Walled Silicon Nanotube Battery Anodes through Solid-Electrolyte Interphase Control. *Nature Nanotechnol.* **2012**, *7*, 310–315.
37. Yao, Y.; Liu, N.; McDowell, M. T.; Pasta, M.; Cui, Y. Improving the Cycling Stability of Silicon Nanowire Anodes with Conducting Polymer Coatings. *Energy Environ. Sci.* **2012**, *5*, 7927–7930.
38. Park, O.; Lee, J.-I.; Chu, M.-J.; Yeon, J.-T.; Yoo, S.; Choi, S.; Choi, N.-S.; Park, S. High-Performance Si Anodes with a Highly Conductive and Thermally Stable Titanium Silicide Coating Layer. *RSC Adv.* **2013**, *3*, 2538–2542.
39. Nakai, H.; Kubota, T.; Kita, A.; Kawashima, A. Investigation of the Solid Electrolyte Interphase Formed by Fluoroethylene Carbonate on Si Electrodes. *J. Electrochem. Soc.* **2011**, *158*, A798–A801.
40. Song, J.; Lee, S. J.; Kim, Y.; Kim, S.-S.; Lee, K. T.; Choi, N.-S. Thermal Reactions of Lithiated and Delithiated Sulfur Electrodes in Lithium-Sulfur Batteries. *ECS Electrochem. Lett.* **2014**, *3*, A26–A29.